



Shape-controlled fabrication of TiO₂ hollow shells toward photocatalytic application

Hamed Eskandarloo, Meisam Zaferani, Arkaye Kierulf, Alireza Abbaspourrad*

Department of Food Science, College of Agriculture & Life Sciences, Cornell University, 243 Stocking Hall, Ithaca, NY 14853, USA

ARTICLE INFO

Keywords:

Microfluidic approach
Titanium dioxide
Hollow shell
Well-defined shape
Photocatalytic activity

ABSTRACT

This paper introduces a droplet-based microfluidic approach, followed by several post-treatments, for the fabrication of TiO₂ hollow shells with novel morphology and perfectly uniform size distribution, which were further decorated with platinum nanostructures to improve their photocatalytic activity and their ability to remove organic pollutants. In particular, a single-emulsion technique was used to emulsify an oil phase containing a titanium dioxide precursor, titanium *n*-butoxide (TBT), and a UV-curable polymer resin, trimethylolpropane triacrylate (ETPTA), into an aqueous phase. These emulsion droplets then readily underwent phase separation and sol-gel reaction at the emulsion interface, forming a TiO₂ shell that would eventually rupture, release the ETPTA core, and form an anatase TiO₂ hollow shell after UV, isopropanol, and thermal post-treatments. Compared with TiO₂ hollow spheres reported in the literature, the TiO₂ hollow shells produced here have a well-defined inner cavity that significantly improves their photocatalytic activity and allows for the selective introduction of advanced functions by the addition of metal co-catalysts like platinum. This new approach, by offering the ability to uniformly control the shape of the TiO₂ photocatalyst and the ability to selectively introduce co-catalysts, offers an alternative platform for the design and fabrication of high-performance photocatalysts for efficient water purification.

1. Introduction

The ability to harness the sun's energy has such wide-ranging implications that different ways to efficiently do so are continually being pursued worldwide. Semiconductor-based photocatalysis is one efficient approach in chemically harnessing the sun's free, abundant energy [1,2]. Unfortunately, inefficient light-harvesting design and the recombination of photo-generated charge carriers limit the performance of these photocatalysts [3]. Thus, the development of functional photo-responsive materials that provide both efficient light-harvesting capabilities and charge carrier separation is the main challenge to be overcome in current photocatalyst design.

TiO₂ photocatalysts with a hollow structure, in particular, have received considerable attention in recent years owing to their unique properties [4–7]. First, the thin shell of these hollow materials provides shorter charge carrier lengths, decreasing the probability that electron-hole recombination reactions occur before active charges reach the surface of the material where actual catalytic turnovers take place. Second, hollow structures have high porosity within their walls, which reduces the diffusion length and increases their accessibility to reactants because of a higher number of active sites. Third, in hollow

structures with a wall thickness smaller than the light penetration depth, the voluminous void space improves radiation absorption efficiency through “light trapping” effects. Plain structure, non-hollow, spherical particles can absorb only a small fraction of incident light because the rest is reflected. But in the case of hollow materials, multiple scattering events could occur within the interior cavity of a single particle, which are expected to improve the overall absorption efficiency, thereby contributing to enhanced light-harvesting abilities [8–12].

Aiming to improve photocatalytic activity in this way, a few studies have recently been published detailing the fabrication of TiO₂ hollow shells with a well-defined hollow cavity. Enhanced photocatalytic activity and improved diffusion of the reactant molecules onto the active surface were demonstrated using these hollow shell structures. Typically, these TiO₂ hollow shells were fabricated via templating or ripening processes [13–17]. The high reactivity of titanium precursors towards hydrolysis-condensation reactions, however, makes it challenging to fabricate these TiO₂ hollow structures in a controlled manner. Thus, the fabrication of TiO₂ hollow shells with a well-defined shape for efficient photocatalysis remains an important yet unmet need. One promising strategy to potentially resolve this issue is the use of

* Corresponding author.

E-mail address: alireza@cornell.edu (A. Abbaspourrad).

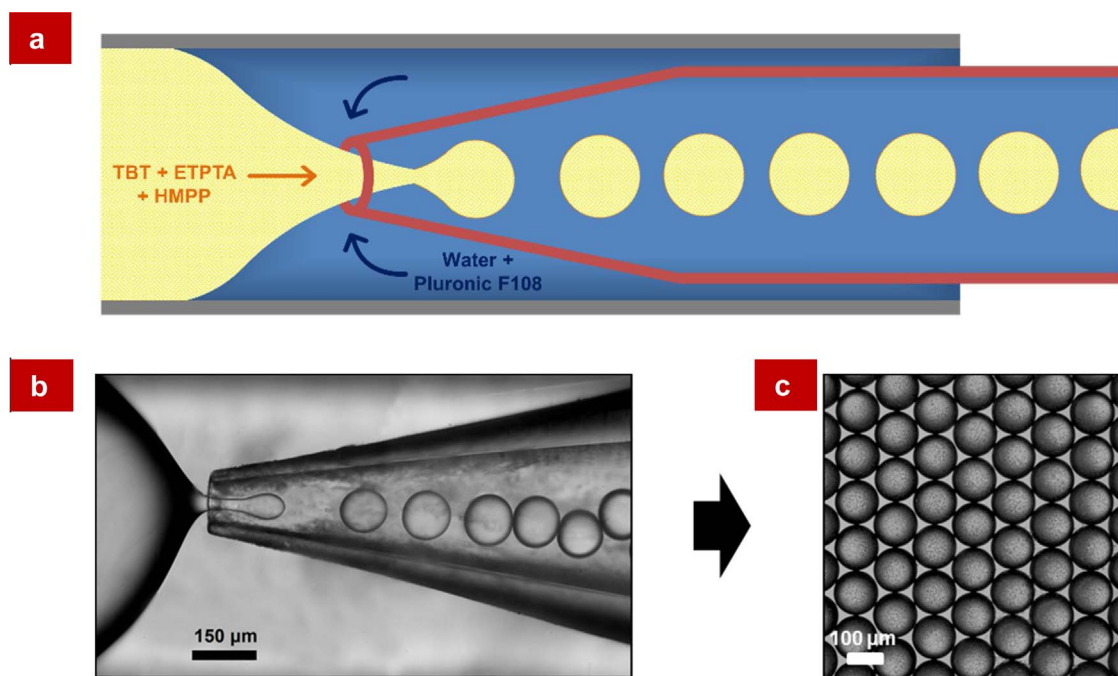


Fig. 1. (a) Schematic illustration of the microfluidic device composed of an outer square capillary for the injection of both oil and aqueous phases and an inner tapered, circular capillary for droplet collection. (b) Optical microscope image showing droplet generation in dripping mode. (c) Optical microscope image of resultant droplets.

high-throughput microfluidic devices. In the past, capillary microfluidic devices have been shown to produce highly monodisperse emulsion droplets, uniform-sized spherical colloidal nanomaterials, polymer microcapsules, hydrophobic porous particles, and monodisperse hollow spheres [18–25]. While this microfluidic approach has not yet been used to fabricate TiO_2 hollow shells, the precise control over particle shape and size that this approach offers could potentially give many advantages over previous approaches.

In this paper, we introduce a TiO_2 catalyst with a new morphology that offers several advantages for photocatalytic application owing to its special configuration. We use a droplet-based microfluidic approach, followed by UV-exposure and other post treatments, to fabricate TiO_2 hollow shells with well-defined shape. These fabricated hollow shell structures could then serve as host for functional co-catalysts such as metal nanostructures, which could further improve photocatalytic activity. Recent reports show that one such metal, in particular–platinum (Pt)–can completely extract excited electrons from a semiconductor [26,27]. This ability to efficiently deplete excited electrons, together with its well-known superior catalytic activity, makes Pt a good potential co-catalyst. With this in mind, we decorated the outer surface and the interior cavity of the TiO_2 hollow shells with Pt to improve their photocatalytic activity. With these great features, Pt-decorated TiO_2 shells show promise as an alternative way to more efficiently remove organic pollutants such as Methylene Blue (MB) from aqueous solutions.

2. Materials and methods

2.1. Materials

Titanium *n*-butoxide (TBT), ethoxylated trimethylolpropane triacrylate (ETPTA), 2-hydroxy-2-methyl-1-phenyl-1-propanone (HMPP), Pluronic F108, chloroplatinic acid, sodium borohydride, isopropanol (i-PrOH), and MB were all of analytical grade quality and purchased from Sigma–Aldrich.

2.2. Characterization methods

Crystallographic analysis was carried out by X-ray diffraction (XRD) using $\text{Cu K}\alpha$ radiation ($\lambda = 0.15478 \text{ nm}$) (Bruker Eco D8 Advance AXS system). The production of emulsion drops is observed using an inverted optical microscope (DMIL LED, Leica) equipped with a high-speed camera (MicroLab 3a10, Vision Research). The surface morphology and distribution of the microparticles were observed by using a field-emission scanning electron microscope (SEM, LEO FESEM, LEO 1550) equipped with an Energy-Dispersive X-ray spectroscopy (EDS) system for analyzing the chemical composition of the samples. The particle size and distribution of the Pt nanoparticles were obtained by high-resolution transmission electron microscopic (HRTEM, FEI-F20-TEM-STEM, 200 kV) studies. X-ray photoelectron spectroscopy (XPS) was used to study the chemical state of samples using a Surface Science Instruments Model SSX-100 XPS system. Fourier Transform-Infrared Spectroscopy (FTIR) spectra was recorded at the $4000\text{--}400 \text{ cm}^{-1}$ region on Shimadzu FTIR Model-IRAffinity-1S (MIRacle 10). Photoluminescence (PL) emission spectra were recorded using a Spectrofluorophotometer (RF-6000, Shimadzu) with excitation wavelength at 320 nm. UV–vis diffuse reflectance (DRS) was measured using a UV–vis spectrophotometer (Shimadzu, UV-2600) equipped with an integrating sphere unit (Shimadzu, ISR-2600 Plus). The total organic carbon (TOC) measurements were carried out using a TOC analyzer (Model 1010, OI Analytical, College Station, TX).

2.3. Photocatalytic experiments

Photocatalytic removal experiments were carried out at room temperature in a batch quartz reactor. Artificial irradiation was provided by an 8 W mercury lamp (model UVLS-28 EL Series) emitting at around 356 nm, situated on top of the batch quartz reactor. The distance between the solution surface and the light source was 10 cm. In each test, 40 mg of catalyst suspension, dispersed in water for 15 min using an ultrasonic bath (Symphony™ Ultrasonic Cleaners, VWR, 35 kHz, 144 W), and 10 mg L^{-1} of MB were transferred into the reactor and stirred for 30 min to achieve the adsorption equilibration in the dark before irradiation. The photocatalytic reaction was started by turning on the light

source. At the given irradiation time, a sample (5 mL) was taken out from the solution and then MB concentration was measured by UV–vis spectrophotometer (Shimadzu, UV-2600) at $\lambda_{\text{max}} = 665 \text{ nm}$.

3. Results and discussion

As shown in Fig. 1a, a capillary microfluidic device was used to emulsify the oil phase, which contained the TiO_2 precursor and other components, in an aqueous phase. The oil phase contained a titanium precursor–3.5 wt.% TBT–and a UV-curable polymer resin with its photo-initiator–ETPTA and HMPP, respectively. The aqueous phase contained 1 wt.% triblock copolymer Pluronic F108, an emulsion stabilizer. The microfluidic device was composed of an inner cylindrical glass capillary (World precision instruments, Inc., GR100-6) of 1 mm outer diameter, tapered using a micropipette puller (Sutter instrument, P-97), which was inserted into a square capillary (Harvard borosilicate square tubing) with a slightly larger inner diameter of 1.05 mm. The oil and aqueous phases were injected through the opposite ends of the outer square capillary. The aqueous phase flowing from the right, passing through the annulus region between the two capillaries, swept and broke up the oil phase streaming from the left, producing highly monodisperse emulsion drops that were then collected by the inner cylindrical capillary. The emulsions so generated were then collected in an aqueous solution of 1 wt.% tri-block copolymer Pluronic F-108. Flow rates of oil and continuous phases were 50 and 900 $\mu\text{L}/\text{h}$, respectively and manipulated to modulate the volume ratio of the oil phase in the water phase, such that a stable dripping mode was produced (Fig. 1b). The emulsion drops generated were uniform in size ($\sim 130 \mu\text{m}$) and shape as shown in Fig. 1c.

After the droplets were generated from the microfluidic device, a mixture-driven phase separation readily occurs because of the low miscibility between TBT and ETPTA. TBT naturally migrates outward to form a layer around the ETPTA core in order to reduce the high interfacial tension between ETPTA and the surrounding water, eventually resulting in a core-shell morphology after 4 h. At the interface in contact with water, highly reactive TBT undergoes hydrolysis, and through a sol-gel reaction, forms a thin Ti–O–Ti shell around the ETPTA core, as schematically illustrated in Fig. 2a. Over time, because TBT is hydrophilic, it continues to migrate outward to the interface between the oil and the shell, and water that diffuses into this interface from outside continues to hydrolyze it and crosslink the shell [28]. This conversion from liquid TBT to solid, amorphous TiO_2 leads to a decrease in volume—a continuous shrinkage of the shell around the incompressible ETPTA core that eventually ruptures the thinnest part of the shell due to mounting pressure, and expels the ETPTA droplet, resulting in an anisotropic particle with snowman morphology. Statistical size distribution histograms show that after 24 h, the size of these TiO_2 shells decreased from 130 to 88 μm and the size of the ETPTA droplet released increased from 17 to 68 μm , as illustrated in Fig. 2b. Although the droplets were monodisperse and subjected to the same incubation conditions, oil expulsion occurred within a rather wide 4–6 h window for a single sample; this could be due to small variations in the rate of hydrolysis, crosslinking, and shell thickness. Preliminary experiments showed that a low concentration of TBT indeed led to such shell rupture. A schematic diagram of this series of steps, alongside their corresponding optical microscope images, are shown in Fig. 3a–b.

As ETPTA continues to be expelled, the snowman morphology slowly morphs into a peanut shape after 10–24 h, as shown in Fig. 3a–b. Formation of these amorphous TiO_2 shells, completed within 24 h, was confirmed by FTIR studies as shown under Supporting information, Fig. S1. The ETPTA core being expelled at the peanut morphology step was then solidified by UV light (365 nm, 8 W, model UVLS-28 EL Series) exposure. Subsequent i-PrOH washing removed the solidified ETPTA from the TiO_2 shells. The amorphous TiO_2 shells thus isolated were then freeze-dried. Finally, upon thermal treatment at 500 °C for 1 h, any remaining polymerized ETPTA inside the shells were removed by

burning, and the amorphous TiO_2 hollow shells were transformed from the amorphous phase to the anatase phase, solidifying it. After this thermal treatment, the hollow shells shrank to about half their initial diameter.

How the microfluidic-produced emulsion transforms into a core-shell morphology is an interesting step that can be elucidated by a theoretical, diffusion model. Taking our starting point $t = t_0$ as the initial formation of a thin shell of TiO_2 around the emulsion to quickly minimize ETPTA/water interfacial tension (Fig. 4a), the outward diffusion of TBT afterwards, or its rate of change of concentration, can be modelled using Fick's second law [29]:

$$\frac{\partial C}{\partial t} = D_{\text{eff}} \nabla^2 C \quad (1)$$

which can be simplified, due to the emulsion's spherical symmetry, to [30]

$$\frac{\partial C}{\partial t} = D_{\text{eff}} \frac{1}{r^2} \frac{\partial}{\partial r} \left(r^2 \frac{\partial C}{\partial r} \right) \quad (2)$$

At $t = t_0$, as shown in Fig. 4a, ETPTA composes the innermost phase, a homogeneous mixture of ETPTA/TBT composes the middle layer, and a thin layer of TiO_2 composes the outermost shell. Over time, TBT from the middle layer further diffuses outward radially—to minimize ETPTA/water interfacial tension—at a rate in proportion to the diffusion coefficient, D_{eff} . The TBT that diffuses outward at a current I_{out} that varies with time then gets adsorbed into the outermost shell where it becomes hydrolyzed into TiO_2 , increasing shell thickness. This outward TBT diffusion from the middle layer induces the ETPTA from the middle layer to concurrently diffuse inward, in the opposite direction, into the innermost ETPTA core, which therefore grows in size, $R(t)$, and would eventually result in a threshold size. Eq. (2) can be solved with a finite element method using COMSOL Multiphysics and its live link with MATLAB. In Fig. 4b–d, snapshots at three different points in this diffusion process are shown. Once the threshold size of the ETPTA core is reached, it is expelled from the shell to form a snowman/peanut morphology, whose shapes can also be modelled, this time by using *Surface Evolver* (see Supporting information, Fig. S2).

The TiO_2 hollow shells produced after the three post-treatments (UV exposure, i-PrOH washing, 500 °C heating) were then studied by optical microscopy and SEM, which showed that they had a well-defined morphology, a uniform diameter of about 50 μm , and a cavity with a diameter of about 18–22 μm (Fig. 5a–c). XRD analysis further showed that all the XRD reflections could be fully assigned to TiO_2 in the crystallized anatase phase (JCPDS, No. 21–1272), as shown in Fig. 5d. It is well-known that anatase TiO_2 exhibits photocatalytic activity superior to that of other polymorphs, due to its ability to suppress the recombination of photogenerated charge carriers and thus increase their number [31]. The average crystal sizes of as-prepared TiO_2 and thermally treated TiO_2 hollow shells calculated using Scherrer's formula ($d = K\lambda/\beta\cos\theta$, where d is the crystal size, K is equal to 0.89, λ is the X-ray wavelength, β is the width in radians of the reflection, and θ is the Bragg angle) from the most intense (1 0 1) reflection, are around 10 and 28 nm, respectively.

Due to the special configuration of these TiO_2 hollow shells, Pt nanostructures could even be embedded onto both their outer surface and interior cavity to further improve their photocatalytic activity. Using a typical co-catalyst loading process, these anatase TiO_2 shells could be decorated with metallic Pt through a conventional chemical reduction method, using NaBH_4 as reductant that would readily reduce a Pt^{4+} precursor into metallic Pt nanostructures. The ability of a chemical reduction method to produce small and homogeneous metal nanoparticles with a good distribution on a support surface has been described [32]. For this purpose, the TiO_2 hollow shells produced in this study were suspended in an aqueous H_2PtCl_6 solution, then a NaBH_4 solution (50 mg L^{-1}) was added dropwise to the vigorously stirred reaction mixture for 1 h. The samples were then dried in an air oven at

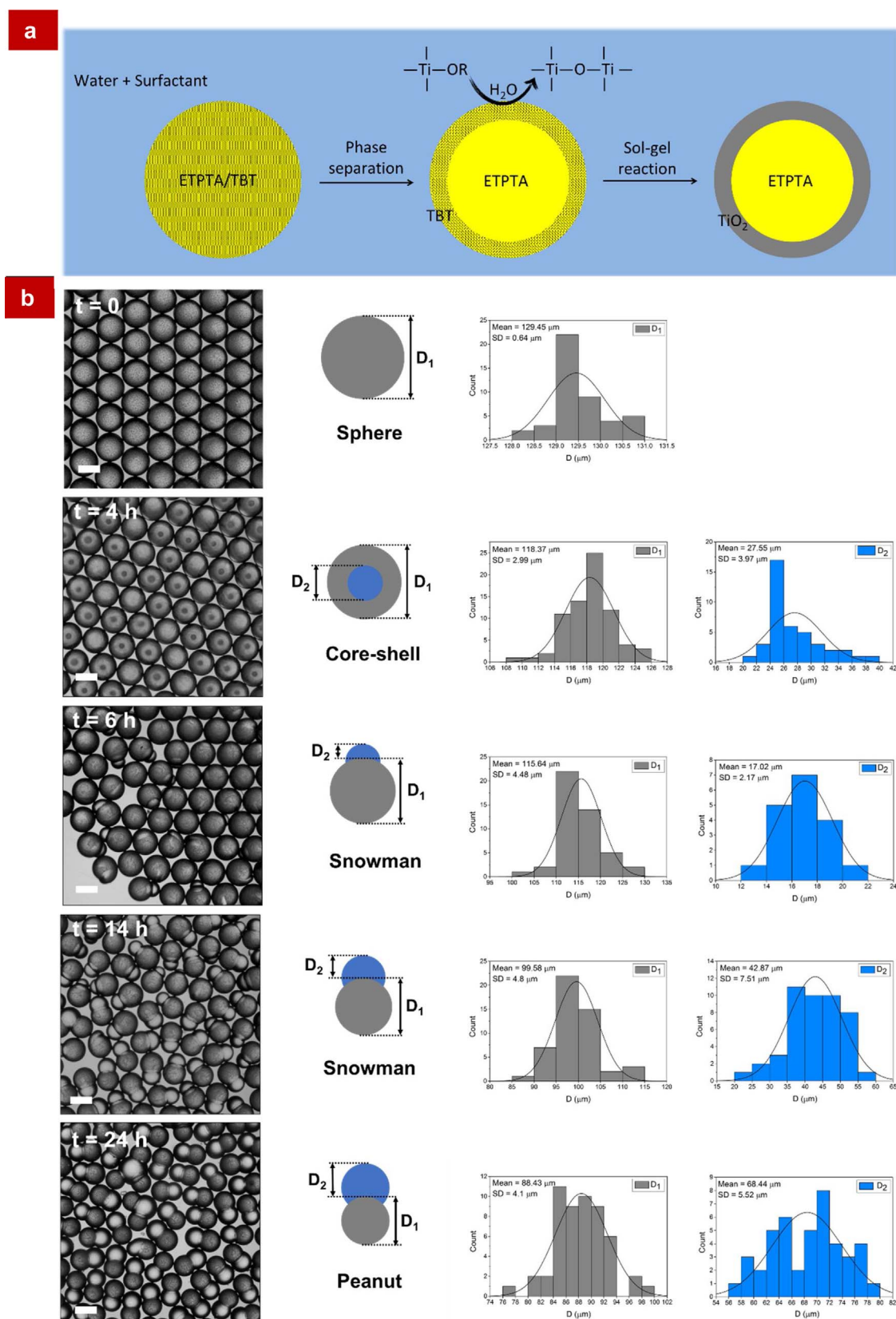


Fig. 2. (a) Schematic diagram illustrating mixing-induced phase separation and sol-gel reaction of titanium alkoxide precursor at the emulsion interface in contact with aqueous medium for an emulsion droplet containing ETPTA and TBT. (b) Series of optical microscope images and schematic diagrams illustrating the sequential steps of shell rupture and the release of the oil, and histograms describing size distribution of the droplets over time, resulting in a snowman/peanut morphology (Scale bar represents 100 μm).

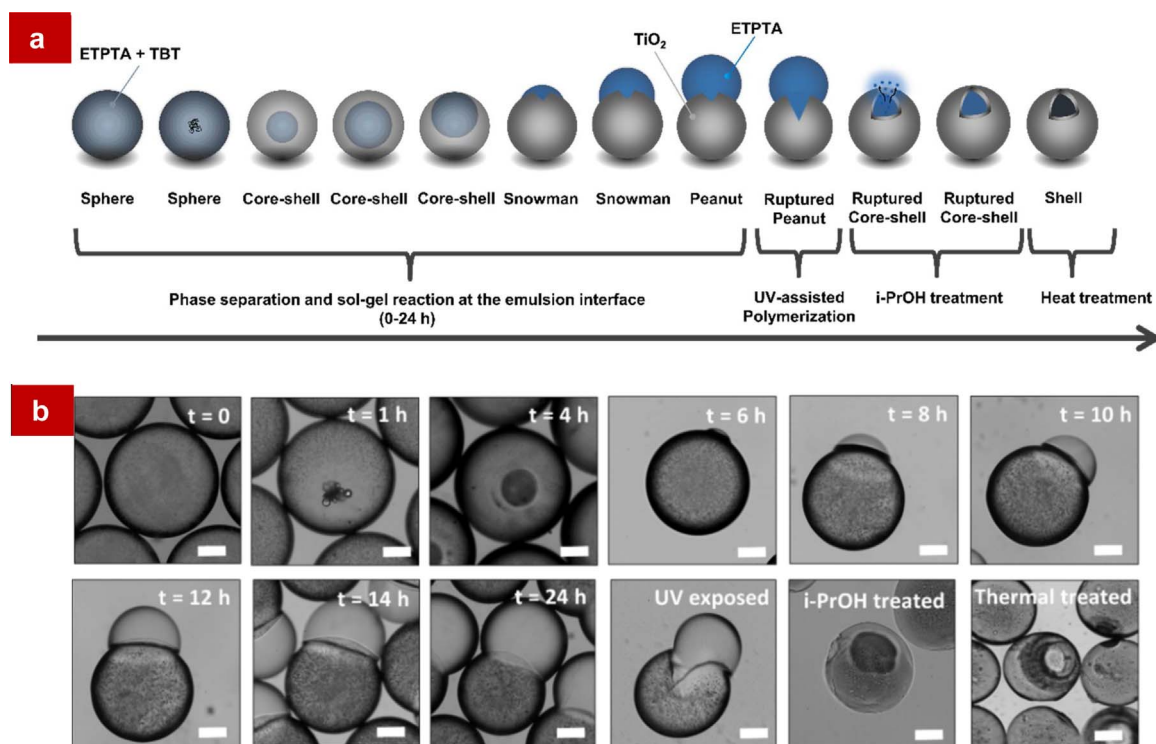


Fig. 3. (a) Schematic diagrams and (b) series of optical microscope images illustrating the sequential steps of shape-controlled formation of a single TiO_2 hollow shell from an emulsion droplet containing ETPTA and TBT in aqueous phase (Scale bar represents 30 μm).

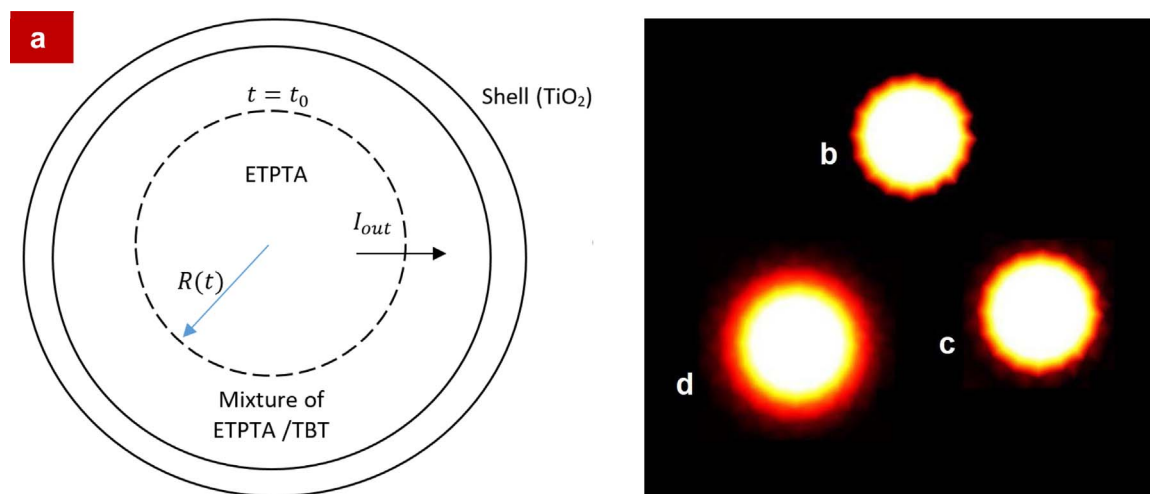


Fig. 4. (a) Schematic of the model. The hierarchical structure of the droplet at time $t = t_0$ is shown, where diffusion of TBT starts at $t = 0$. $R(t)$ with current of I_{out} will increase until it reaches a threshold value. (b) Shell at its inception, (c) the thickness of the shell is becoming greater, and (d) thickness gets its threshold value.

80 $^{\circ}\text{C}$ for 10 h. XRD analysis after this treatment indicated that the Pt-decorated TiO_2 shells show a higher reflectance intensity than both as-prepared TiO_2 and undecorated TiO_2 hollow shells (Fig. 5d), which could be attributed to the fine dispersion of the Pt nanostructures. An SEM image further showed that the Pt nanoparticles aggregated into nanoclusters on the shell surface (Fig. 6a), which occurred because metal nanoparticles inherently tend to aggregate because of their high specific surface energy [33]. From the TEM image (Fig. 6b), it is clear that Pt nanoparticles were well decorated on the surface of the TiO_2 shell. The mean diameter of these Pt particles was about 10 nm. An HRTEM image (Fig. 6c) shows two different lattice planes with spacing of 0.351 and 0.224 nm. These two planes corresponded to the (1 0 1) plane of anatase TiO_2 and the (1 1 1) plane of metallic Pt, respectively. The EDS technique was used for the elemental analysis of samples (see

Supporting information, Fig. S4). EDS analysis indicated that Pt resided on both the outer surface and the interior cavity of the TiO_2 shell. The same amount of Pt could be detected on different areas of the shell, which indicated a uniform distribution. To further investigate the existence of Ti, O, and Pt elements in the resultant samples, EDS elemental mapping analysis was performed. As shown in Fig. 6d–f, it is clear that the elements Ti, O, and Pt are present in the resultant Pt-decorated TiO_2 shell. The results show that Pt nanoparticles are distributed throughout the surface of the shell.

In addition, XPS was used to verify that these Pt-decorated TiO_2 shells were indeed metallic. Fig. 6g shows a high-resolution XPS spectrum of the Pt-decorated TiO_2 shells in the Pt 4f region. The Pt 4f signal was deconvoluted into two components. The binding energies of two pairs of doubles were located at 71.45, 74.8 eV and 73.9, 77.25 eV,

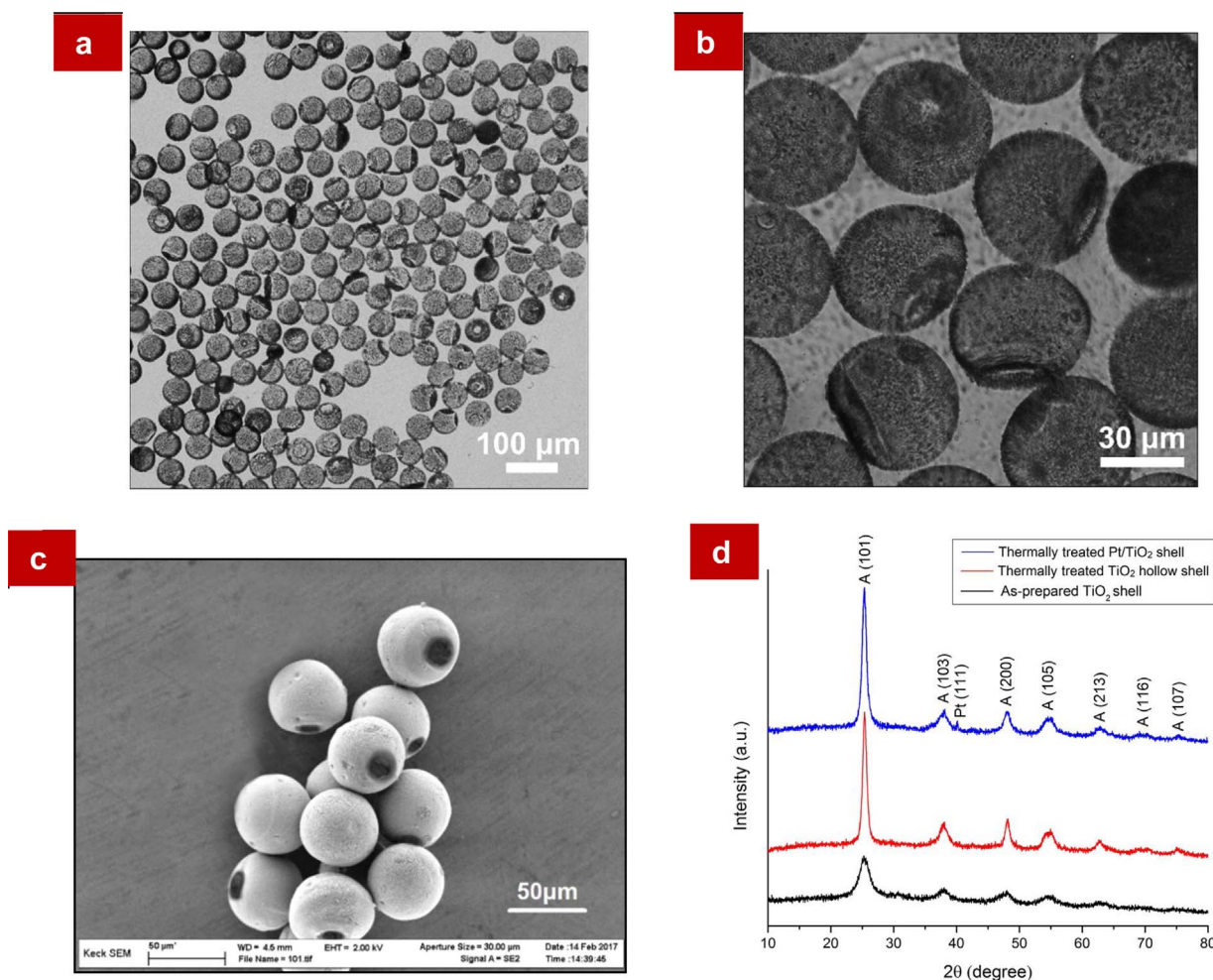


Fig. 5. (a–b) Optical microscope images and (c) SEM micrograph of TiO₂ hollow shells at different magnifications. (d) XRD patterns of as-prepared TiO₂, thermally treated TiO₂ hollow shells, and thermally treated Pt-decorated TiO₂ shells at 500 °C.

which were assigned to Pt 4f_{7/2} and Pt 4f_{5/2} of Pt⁰ and Pt^{IV}O₂ species, respectively. The percentage of the Pt⁰ species, calculated from the relative peak areas, was 76.9%. For photocatalytic reactions, metallic platinum can act as a reactive site and provide many more active sites than other oxidation states of platinum such as PtO [34]. Moreover, the presence of TiO₂ was also identified by the XPS spectra (Fig. 6h). The binding energies located at around 457.85 and 463.55 eV—corresponding to Ti 2p_{3/2} and Ti 2p_{1/2}, respectively—were attributed to Ti⁴⁺. All these results—combined—verify that the droplet-based microfluidic approach used here, followed by all the post-treatments, was able to successfully fabricate uniform-sized anatase TiO₂ shells with a well-defined shape and decorated with metallic Pt nanostructures.

After fabrication, we evaluated the photocatalytic properties of our TiO₂ catalysts by testing their efficiency in removing pollutants under UV-A (365 nm) light irradiation, using MB as a model organic pollutant. For comparison purposes, we fabricated five different TiO₂ catalysts (Fig. 7a): (i) TiO₂ hollow spheres, which were fabricated by immediately exposing emulsions to UV light right after they were generated by the microfluidic device and thus did not have any cavities; (ii) Pt-decorated TiO₂ hollow spheres, which were hollow spheres decorated with Pt on the outer surface; (iii) TiO₂ hollow shells, which had cavities, and produced as previously described; and two types of shells decorated with Pt—(iv) Pt-decorated TiO₂ hollow shells, which were decorated with Pt only on the outer surface and had an empty cavity; and (v) Pt-decorated TiO₂ shells, which were decorated on both the outer surface and inner cavity. The relative efficiency of these five different types of TiO₂ catalysts at degrading the MB solution at

different irradiation times is shown in Fig. 7b. The absorbance maxima of MB was determined beforehand to be 664 nm (Fig. 8a). It has been shown that MB's absorbance intensity in solution decreased at different rates depending on which catalyst was used to degrade it. The control (no catalyst) showed only a 6% MB removal after UV-A irradiation. All five TiO₂ catalysts showed high photocatalytic activity and their activity follows the order (v) Pt(0.4 wt. %)/TiO₂ shell > (iv) Pt(0.4 wt. %)/TiO₂ hollow shell > (iii) TiO₂ hollow shell > (ii) Pt(0.4 wt. %)/TiO₂ hollow sphere > (i) TiO₂ hollow sphere. Additionally, the removal process followed the pseudo-first-order rate kinetics described as: $\ln(C_0/C) = kt + A$, where k represents the reaction rate constant, and C_0 and C are the concentrations of MB in the solution before and after irradiation, respectively. The kinetics of the MB removal can be described by the Langmuir–Hinshelwood model (a clear linear correlation for MB removal), as illustrated in Fig. 7c. The photocatalytic removal rate constants for (v) Pt(0.4 wt. %)/TiO₂ shell, (iv) Pt(0.4 wt. %)/TiO₂ hollow shell, (iii) TiO₂ hollow shell, (ii) Pt(0.4 wt. %)/TiO₂ hollow sphere, and (i) TiO₂ hollow sphere were 1.51×10^{-2} , 1.3×10^{-2} , 1.05×10^{-2} , 0.87×10^{-2} , and 0.74×10^{-2} , respectively.

In general, all the shell-type structures had more photocatalytic activity than the sphere-type structures, which could be attributed to several possible reasons, as schematically illustrated on the inset of Fig. 8b. Benefiting from its special configuration, the shell structure allows more light and more reactants into its inner cavity, thus increasing the overall surface area, which is highly important for providing more active sites [17,35]. In fact, when the adsorption rates of

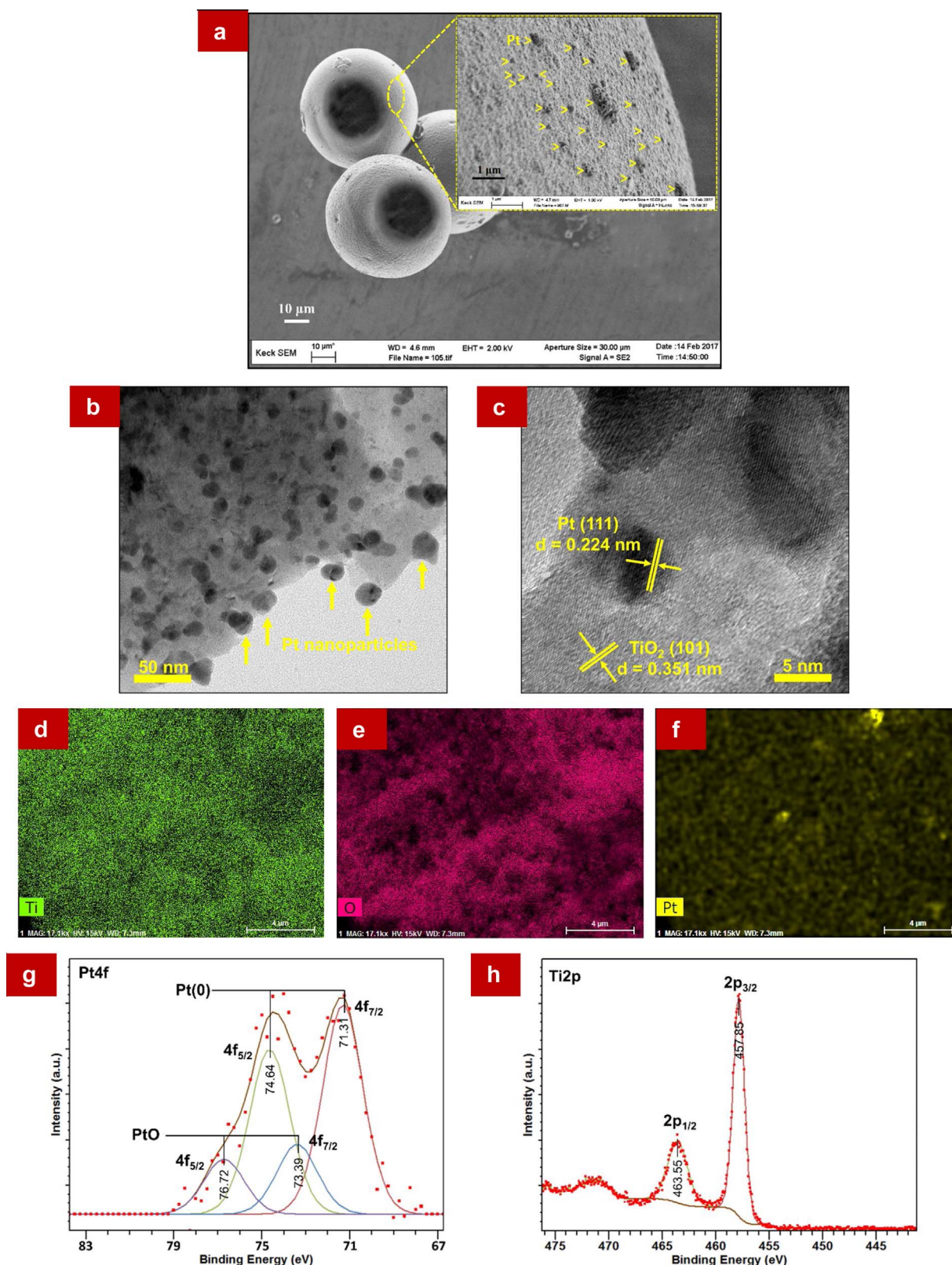


Fig. 6. (a) SEM micrograph of Pt-decorated TiO₂ shells. The inset of (a) is a magnified view of the surface, showing the aggregation of Pt nanoparticles into nanoclusters. (b) TEM, the yellow arrows indicate the Pt nanoparticles, and (c) HRTEM images of Pt-decorated TiO₂ shells. The elemental mapping images of (d) Ti, (e) O, and (f) Pt elements on the surface of a Pt-decorated TiO₂ shell. High-resolution (g) Pt 4f and (h) Ti 2p XPS spectra of the Pt-decorated TiO₂ shells. (For interpretation of the references to colour in this figure legend, the reader is referred to the web version of this article).

MB molecules were tested on both the sphere and shell structures in the dark, it was found that MB tended to adsorb more to the hollow shells that had cavities (14.2%) than to the hollow spheres that had none

(4.7%). The unique shell structure offers a highly porous surface area for better contact between the photocatalyst and target molecules, which has a significant effect on accelerating adsorptive and

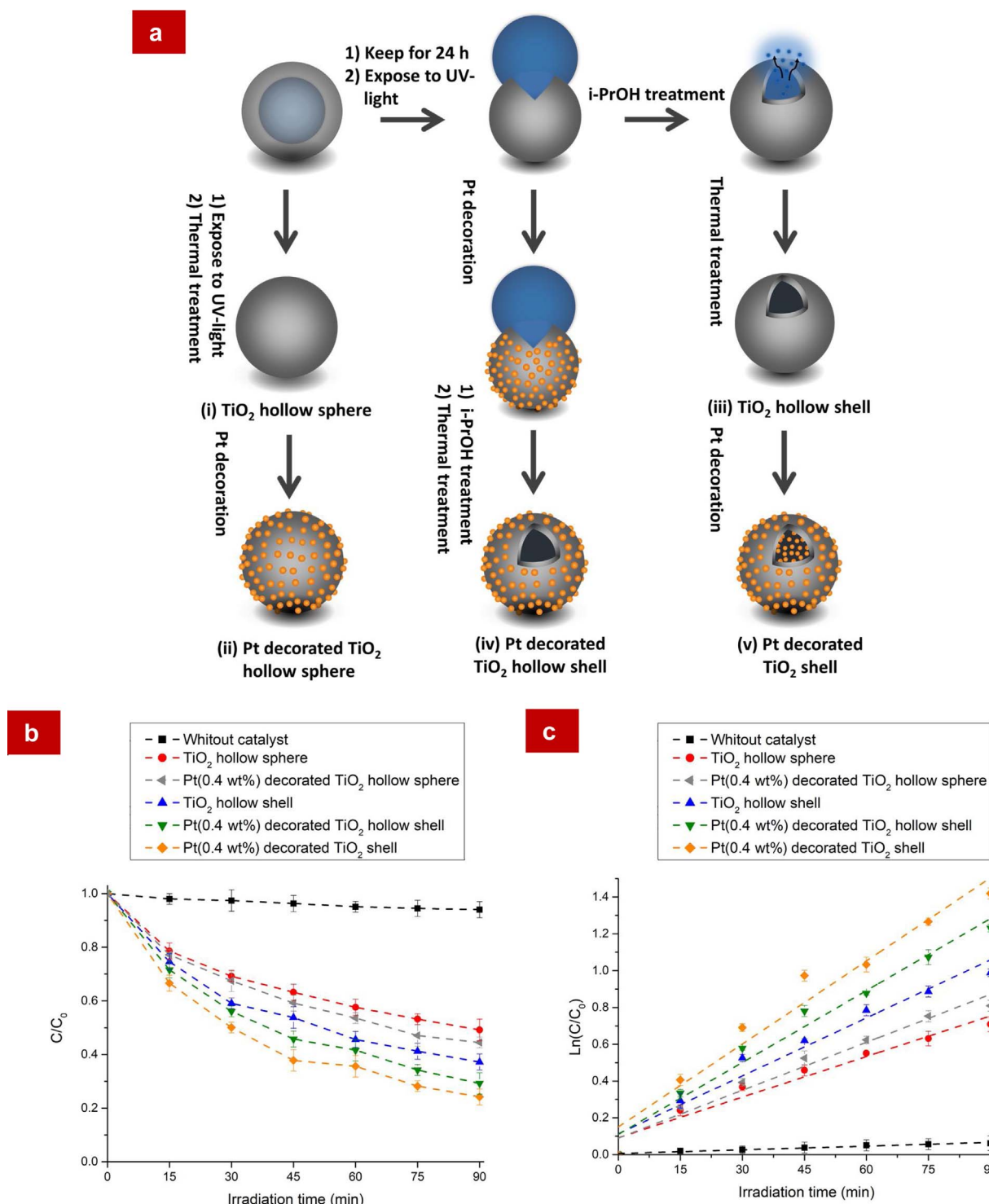


Fig. 7. (a) Schematic of the fabrication of different TiO_2 catalysts for comparison purposes, namely, (i) TiO_2 hollow sphere (no cavity), (ii) Pt-decorated TiO_2 hollow sphere, (iii) TiO_2 hollow shell (with cavity), and two types of Pt-decorated TiO_2 hollow shells—(iv) Pt-decorated TiO_2 hollow shells, decorated with Pt only on the outer surface; and (v) Pt-decorated TiO_2 shells, decorated with Pt on both the outer surface and inner cavity. (b) A plot of C/C_0 changes as a function of irradiation time for a MB solution in the presence of different TiO_2 catalysts, and (c) the corresponding pseudo-first-order kinetic rate plot.

photocatalytic reactions. In addition, the shell structure allows multiple reflections of light within the interior cavity, which improves overall light absorption efficiency. This was supported by a DRS study, which showed that the shell structure had greater reflectance intensity than the sphere structure, indicating that the hollow shell with cavity had better light-scattering ability than the sphere that had no cavity (Fig. 8b).

The results also indicate that Pt-decorated shells had more photocatalytic activity than undecorated shells. Furthermore, the shells decorated on both their outside and inside surfaces showed better pollutant removal than shells decorated only outside. The role played by the Pt co-catalysts on the surface of the TiO_2 semiconductor photocatalyst is extremely important here, because they have good scavenging potential for the electrons photogenerated in the conduction band of the

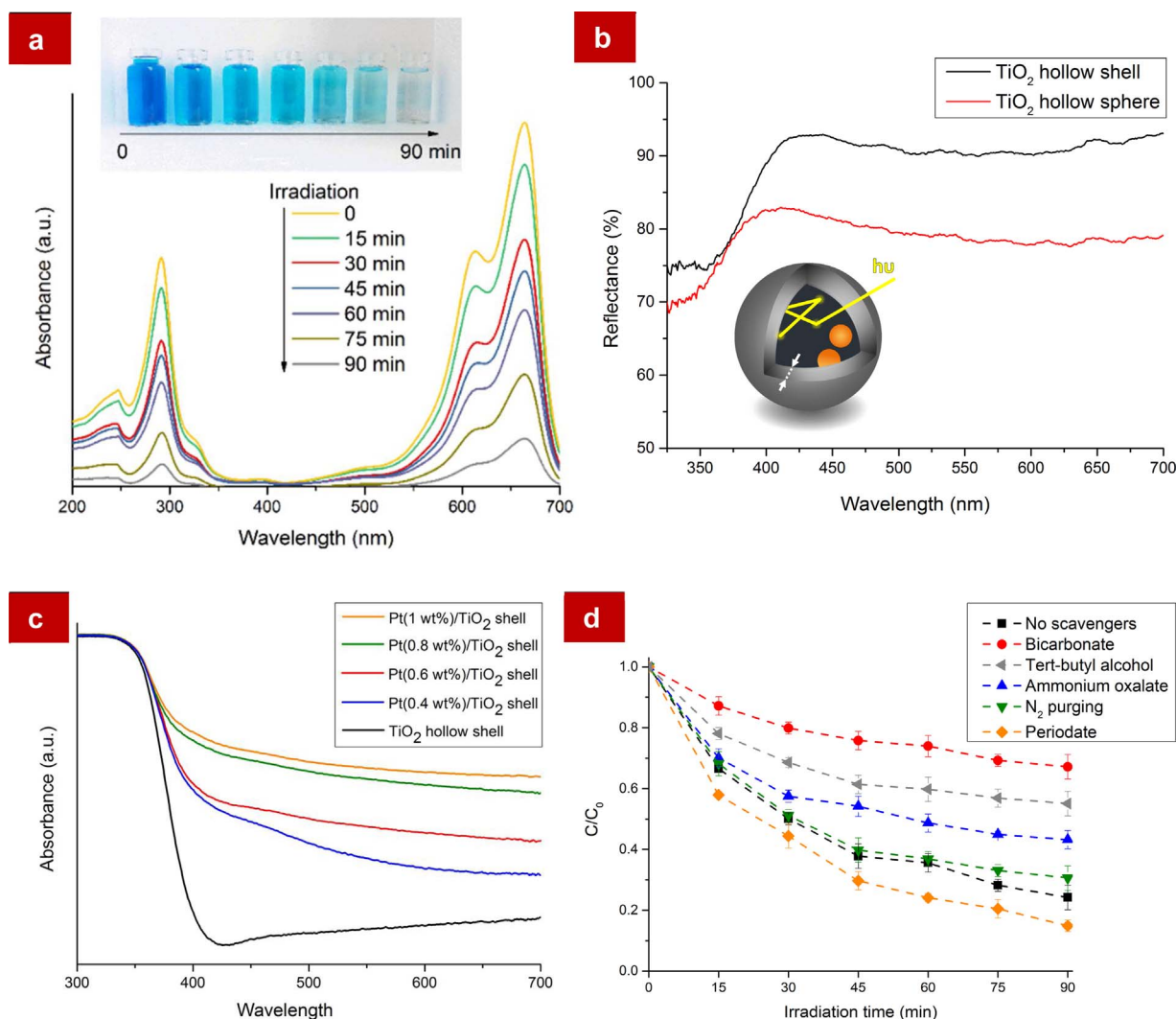


Fig. 8. (a) Changes in UV-vis spectra of MB as a function of irradiation time in the presence of (v) Pt (0.8 wt.%) / TiO₂ shell (The inset is a photo of the corresponding solutions at various times). (b) UV-vis diffuse reflectance spectra of the (i) TiO₂ hollow sphere and (iii) TiO₂ hollow shell structures. The inset of (b) is a schematic illustration of specific properties of the hollow shell structure such as multiple reflections of light within the interior cavity, short charge-transfer length, and the possibility to load Pt co-catalysts within the interior cavity. (c) UV-vis absorption spectra of (iii) TiO₂ hollow shell and (v) TiO₂ shells with different Pt loadings. (d) The effects of various scavengers on the photocatalytic degradation of MB in the presence of (v) Pt (0.8 wt.%) / TiO₂ shell.

semiconductor. The proposed mechanism of charge transfer between the TiO₂ photocatalyst and the Pt co-catalyst is illustrated in Fig. S6 under Supporting information. The Pt co-catalyst can act as an efficient electron trap by the indirect modification of the interfacial charge transfer mechanism. Metal nanostructures typically form Schottky barriers at the metal/TiO₂ interface. Because the Fermi level of Pt is lower than the conduction band of TiO₂, photogenerated electrons can be transferred from the conduction band to the Pt nanostructures decorated on the TiO₂ surface. In fact, the Schottky barrier can trap photogenerated electrons, resulting in the effective separation of electron-hole pairs [36,37]. Therefore, more photogenerated holes can migrate preferentially to the surface of TiO₂ and oxidize the surface-adsorbed H₂O molecules or OH⁻ ions to create very powerful and non-selective oxidizing agents like OH radicals, which are responsible for the decomposition of organic compounds as well as their byproducts [38]. To understand the efficiency of transfer and separation of photogenerated charge carriers by the Pt-decorated TiO₂ shells, PL tests were carried out (see Supporting information, Fig.S3). The decoration of Pt nanostructures generated considerable fluorescence quenching, which suggested that there was indeed a transfer of electrons from TiO₂ to Pt and that there was desirable contact between them [39].

The concentration of Pt decorated on the TiO₂ shell also had an effect on MB removal efficiency. MB removal as a function of irradiation time for the TiO₂ catalysts with different Pt loadings is shown in Fig. S7 under Supporting information. The removal rate of MB increases with increasing Pt loading from 0.4 to 0.8 wt.%. However, when the amount of Pt was above 1 wt.%, no further increase in photocatalytic activity was observed. This may be due to the fact that a further increase in the Pt loading content causes aggregation of Pt nanostructures and growth of these Pt particles during preparation, which act as recombination centers for photogenerated charge carriers. In addition, a higher number of Pt nanostructures can cover the TiO₂ surface and prevent light absorption, decreasing the accessibility of active sites [40,41]. Therefore, the optimal Pt co-catalyst loading is 0.8 wt.% for the Pt/TiO₂ shell.

The impact of Pt decoration on the optical properties of TiO₂ hollow shells was also studied by UV-vis absorption spectroscopy. UV-vis absorption spectra of TiO₂ hollow shells, illustrated in Fig. 8c, presents a steep absorption edge at ~410 nm, which can be associated with the band-gap absorption of TiO₂. Compared to these unloaded (iii) TiO₂ hollow shells, (v) Pt-loaded shells absorb a wider range of wavelength extending into the visible light area, which is called a red-shift. Pt-

loaded catalysts exhibit enhanced visible light absorption, which arises mainly from the localized surface plasmon resonance of the decorated Pt nanostructures. The optical band-gap energy (E_g) values were estimated by extending a line from the maximum slope of the curve to the X-axis, according to the equation of $E_g = hc/\lambda_g$, where λ_g is the optical absorption edge of the semiconductor [42]. The E_g values for the TiO₂ hollow shell and the Pt (0.4, 0.6, 0.8, and 1 wt.%) decorated TiO₂ shells are 3.08, 2.85, 2.8, 2.66, and 2.62 eV, respectively, which shows that light in the visible region ($\lambda > 400$ nm) was able to excite the valance band electrons in all of the catalysts, especially the ones decorated with higher levels of Pt. This suggests that Pt-loaded TiO₂ catalysts can also work under visible light, even in the absence of UV light.

To study the mineralization of MB during photocatalytic degradation, the TOC measurements were carried out at the initial MB concentration of 10 mg L⁻¹ as shown under Supporting information, Fig. S8. The TOC results showed an 81.8% reduction in the TOC value after 180 min of irradiation time in the presence of the Pt(0.8 wt. %)/TiO₂ shell.

For a photocatalytic reaction, the role of active species is very important and has been studied using a number of methods [43–46]. To evaluate the role of reactive species generated during light irradiation of the Pt(0.8 wt. %)/TiO₂ shell in aqueous solution, the effects of some scavengers were studied, as shown in Fig. 8d. The results showed that the removal efficiency of MB (75.8%) in the presence of bicarbonate, tert-butyl alcohol, ammonium oxalate, N₂ purging, and periodate, was changed to 32.8%, 44.9%, 56.8%, 69.4%, and 85.1%, respectively. It was observed that with the addition of bicarbonate, which acts as an h⁺ and OH scavenger, and tert-butyl alcohol, which acts as an OH scavenger, the removal efficiency of MB was significantly decreased as compared to the case where no scavengers were added. Additionally, a marked decrease was also observed in the removal efficiency of MB with the addition of ammonium oxalate, which acts as an h⁺ scavenger. And with the purging of N₂ gas, which acts as an O₂^{•-} scavenger, the removal efficiency was slightly decreased. However, upon the addition of periodate which acts as an e⁻ scavenger the removal efficiency of MB was increased. These results suggest that the h⁺ and especially OH are major reactive species in the photocatalytic activity of the Pt(0.8 wt. %)/TiO₂ shell.

Because catalyst stability is a crucial factor in determining whether they can be used in practical applications, the catalytic stability of the Pt(0.8 wt. %)/TiO₂ shells was also studied (see Supporting information, Fig. S9). The results indicate that the Pt/TiO₂ shells produced in the study were highly stable, even after going through ten successive experimental runs. In addition, because these micro-size structured Pt/TiO₂ shells are bigger compared to nano-size particles typically used in pollutant removal, they are easier to collect and reuse.

4. Conclusion

In this study, a shape-controlled approach was described to produce uniform-sized TiO₂ hollow shells using a capillary microfluidic device, followed by post-treatments. A single-emulsion method was used to emulsify the oil phase containing ETPTA, a UV-curable polymer resin, and TBT, a titanium precursor, into the aqueous phase. After UV, i-PrOH, and thermal treatments, an anatase TiO₂ hollow shell was obtained. The TiO₂ shells generated retained a well-defined morphology with a distinct cavity (18–22 μm) on each sphere, and had a uniform diameter distribution of about 50 μm. These TiO₂ hollow shells were then further decorated with metallic Pt nanostructures through a chemical reduction method. The relative photocatalytic activities of these differently designed catalysts—hollow sphere vs. hollow shell, Pt-decorated vs. undecorated shell, Pt-decorated hollow shell vs. Pt-decorated shell—were then evaluated for the removal of MB. Pt (0.8 wt. %)-decorated TiO₂ shells showed optimal MB removal activity, significantly higher compared to those of the hollow shell and sphere structures, due to unique advantages afforded by their special configuration and the

useful properties of the Pt co-catalyst. By offering the ability to control the shape of the TiO₂ photocatalyst, and the ability to selectively introduce advanced functions to it, the shape-controlled approach described in this study offers a new platform for designing and fabricating high-performance photocatalysts for efficient water purification.

Acknowledgments

This work made use of the Cornell Center for Materials Research's Shared Facilities, which are supported through the NSF MRSEC program (DMR-1719875).

Appendix A. Supplementary data

Supplementary material related to this article can be found, in the online version, at doi:<https://doi.org/10.1016/j.apcatb.2018.01.059>.

References

- [1] J. Schneider, M. Matsuoka, M. Takeuchi, J. Zhang, Y. Horiuchi, M. Anpo, D.W. Bahnemann, *Chem. Rev.* 114 (2014) 9919–9986.
- [2] H. Wang, L. Zhang, Z. Chen, J. Hu, S. Li, Z. Wang, J. Liu, X. Wang, *Chem. Soc. Rev.* 43 (2014) 5234–5244.
- [3] I. Robel, V. Subramanian, M. Kuno, P.V. Kamat, *J. Am. Chem. Soc.* 128 (2006) 2385–2393.
- [4] R. Yang, J. Cai, K. Lv, X. Wu, W. Wang, Z. Xu, M. Li, Q. Li, W. Xu, *Appl. Catal. B* 210 (2017) 184–193.
- [5] Y. Zheng, J. Cai, K. Lv, J. Sun, H. Ye, M. Li, *Appl. Catal. B* 147 (2014) 789–795.
- [6] S. Wang, H. Qian, Y. Hu, W. Dai, Y. Zhong, J. Chen, X. Hu, *Dalton Trans.* 42 (2013) 1122–1128.
- [7] L. Gao, Y. Li, J. Ren, S. Wang, R. Wang, G. Fu, Y. Hu, *Appl. Catal. B* 202 (2017) 127–133.
- [8] L. Mao, Y. Wang, Y. Zhong, J. Ning, Y. Hu, *J. Mater. Chem. A* 1 (2013) 8101–8104.
- [9] G. Prieto, H. Tüysüz, N. Duyckaerts, J. Knossalla, G.H. Wang, F. Schüth, *Chem. Rev.* 116 (2016) 14056–14119.
- [10] C.C. Nguyen, N.N. Vu, T.O. Do, *J. Mater. Chem. A* 3 (2015) 18345–18359.
- [11] X.W.D. Lou, L.A. Archer, Z. Yang, *Adv. Mater.* 20 (2008) 3987–4019.
- [12] Y. Zhao, L. Jiang, *Adv. Mater.* 21 (2009) 3621–3638.
- [13] Z. Zhong, Y. Yin, B. Gates, Y. Xia, *Adv. Mater.* 12 (2000) 206–209.
- [14] J.B. Joo, I. Lee, M. Dahl, G.D. Moon, F. Zaera, Y. Yin, *Adv. Funct. Mater.* 23 (2013) 4246–4254.
- [15] Y. Hu, J. Ge, Y. Sun, T. Zhang, Y. Yin, *Nano Lett.* 7 (2007) 1832–1836.
- [16] H.G. Yang, H.C. Zeng, *J. Phys. Chem. B* 108 (2004) 3492–3495.
- [17] J. Lu, P. Zhang, A. Li, F. Su, T. Wang, Y. Liu, J. Gong, *Chem. Commun.* 49 (2013) 5817–5819.
- [18] A. Abbaspourrad, N.J. Carroll, S.H. Kim, D.A. Weitz, *J. Am. Chem. Soc.* 135 (2013) 7744–7750.
- [19] X. Xie, W. Zhang, A. Abbaspourrad, J. Ahn, A. Bader, S. Bose, A. Vegas, J. Lin, J. Tao, T. Hang, H. Lee, *Nano Lett.* 17 (2017) 2015–2020.
- [20] A. Abbaspourrad, N.J. Carroll, S.H. Kim, D.A. Weitz, *Adv. Mater.* 25 (2013) 3215–3221.
- [21] T.H. Eun, S.H. Kim, W.J. Jeong, S.J. Jeon, S.H. Kim, S.M. Yang, *Chem. Mater.* 21 (2009) 201–203.
- [22] H. Lee, C.H. Choi, A. Abbaspourrad, C. Wesner, M. Caggioni, T. Zhu, S. Nawar, D.A. Weitz, *Adv. Mater.* 28 (2016) 8425–8430.
- [23] C.H. Choi, H. Lee, A. Abbaspourrad, J.H. Kim, J. Fan, M. Caggioni, C. Wesner, T. Zhu, D.A. Weitz, *Adv. Mater.* 28 (2016) 3340–3344.
- [24] S.H. Kim, A. Abbaspourrad, D.A. Weitz, *J. Am. Chem. Soc.* 133 (2011) 5516–5524.
- [25] A. Abbaspourrad, H. Zhang, Y. Tao, N. Cui, H. Asahara, Y. Zhou, D. Yue, S.A. Koehler, L.W. Ung, J. Heyman, Y. Ren, *Sci. Rep.* 5 (2015) 12756–12762.
- [26] P. Yu, X. Wen, Y.C. Lee, W.C. Lee, C.C. Kang, J. Tang, *J. Phys. Chem. Lett.* 4 (2013) 3596–3601.
- [27] H. Eskandarloo, M.J. Selig, A. Abbaspourrad, *Chem. Eng. J.* 335 (2018) 434–442.
- [28] W. Lan, S. Li, J. Xu, G. Luo, *Langmuir* 27 (2011) 13242–13247.
- [29] H. Bruus, *Theoretical Microfluidics*, Oxford University Press, New York, 2008.
- [30] B.J. Kirby, *Micro- and Nanoscale Fluid Mechanics: Transport in Micro-Fluidic Devices*, Cambridge University Press, Cambridge, UK, 2010.
- [31] J.H. Pan, X. Zhang, A.J. Du, D.D. Sun, J.O. Leckie, *J. Am. Chem. Soc.* 130 (2008) 11256–11257.
- [32] H. Eskandarloo, A. Badiei, M.A. Behnajady, G. Mohammadi Ziarani, *Photochem. Photobiol.* 91 (2015) 797–806.
- [33] Y. Zhang, Q. Huang, Z. Zou, J. Yang, W. Vogel, H. Yang, *J. Phys. Chem. C* 114 (2010) 6860–6868.
- [34] L. Nie, J. Yu, X. Li, B. Cheng, G. Liu, M. Jaroniec, *Environ. Sci. Technol.* 47 (2013) 2777–2783.
- [35] Z. Pei, L. Ding, H. Lin, S. Weng, Z. Zheng, Y. Hou, P. Liu, *J. Mater. Chem. A* 1 (2013) 10099–10102.
- [36] J. Schneider, M. Matsuoka, M. Takeuchi, J. Zhang, Y. Horiuchi, M. Anpo, D.W. Bahnemann, *Chem. Rev.* 114 (2014) 9919–9986.
- [37] Y. Shiraishi, H. Sakamoto, Y. Sugano, S. Ichikawa, T. Hirai, *ACS Nano* 7 (2013)

- 9287–9297.
- [38] X.J. Yang, X.M. Xu, J. Xu, Y.F. Han, J. Am. Chem. Soc. 135 (2013) 16058–16061.
- [39] K.M. Parida, A. Nashim, S.K. Mahanta, Dalton Trans. 40 (2011) 12839–12845.
- [40] H. Eskandarloo, M. Hashempour, A. Vincenzo, S. Franz, A. Badiei, M.A. Behnajady, M. Bestetti, Appl. Catal. B 185 (2016) 119–132.
- [41] H. Huang, D.Y. Leung, D. Ye, J. Mater. Chem. 21 (2011) 9647–9652.
- [42] K.M. Reddy, S.V. Manorama, A.R. Reddy, Mater. Chem. Phys. 78 (2003) 239–245.
- [43] H. Eskandarloo, A. Badiei, M.A. Behnajady, A. Tavakoli, G.M. Ziarani, Ultrason. Sonochem. 29 (2016) 258–269.
- [44] R. Qiao, M. Mao, E. Hu, Y. Zhong, J. Ning, Y. Hu, Inorg. Chem. 54 (2015) 9033–9039.
- [45] J. Li, Y. Xie, Y. Zhong, Y. Hu, J. Mater. Chem. A 3 (2015) 5474–5481.
- [46] R. Rameshbabu, R. Vinoth, M. Navaneethan, Y. Hayakawa, B. Neppolian, CrystEngComm 19 (2017) 2475–2486.